ADVANCED FUNCTIONAL MATERIALS
www.afm-journal.de

Programmable Arrays of "Micro-Bubble" Constructs via Self-Encapsulation

*Chunhong Ye, Dhaval D. Kulkarni, Hongqi Dai, and Vladimir V. Tsukruk**

The fabrication of ordered arrays of self-encapsulated "micro-bubble" material constructs based on the capillary-driven collapse of flexible silk fibroin sheets during propagation of the diffusion front of the encapsulated material is demonstrated. The individual micro-bubbles of different shapes are composed of a sacrificial material encapsulated within the ultrathin silk coating, which covers and seals the inner material during dissolution of supporting layer. The array of microscopic rectangular multi-layer silk sheets on supporting polymer layers can be selectively dissolved along the edges to initiate their self-encapsulation. The resulting micro-bubble morphology, shape, and arrangements can be readily pre-programmed by controlling the geometry of the silk sheets, such as thickness, dimension, and aspect ratio. These micro-bubble constructs can be utilized for encapsulation of various materials as well as nanoparticles in a single or multi compartmental manner. These biocompatible and biodegradable micro-bubble constructs present a promising platform for one-shot spatial and controllable loading and locking material arrays with addressable abilities.

1. Introduction

Microcapsules or microcontainers with site-specific organized arrangements and timely activated loading-unloading abilities constitute a promising platform for the development of a new generation of ultrasensitive sensors, drug delivery systems for biological and biomedical applications, and for food industry.[1–8] Due to the controlled permeation of components through the wall, microcapsules and microcontainers can be used to encapsulate cells, nanoparticles, polymers, or work as biosensors.[9–11] Thin-shell microcapsules fabricated by layer-by-layer (LbL) assembly are intensely exploited for encapsulation and releasing processes, [12–14] as well as, controlled permeability in response to specific external triggers such as pH,[15] temperature,[16] light,[17] ionic strength,[18] and redox potential [19] by employing a variety of weak intermolecular interactions such as ionic paring,[20] hydrogen bonding,[21] covalent bonding[22] and specific recognition [23]. However, the spatial and temporal control of the release process with a small and precisely defined quantity is one of the premier challenges in the development of delivery arrays with encapsulated materials.[3,24,25]

In addition, the facile fabrication of ordered arrays of pre-loaded microcapsules by immobilization on patterned surfaces through physical entrapment, biochemical or electrostatic interaction, ink-jet printing, or capillary force lithography is challenging and requires multistep procedures.[26–31] The poor stability of microcapsules under harsh conditions is another major limitation for the application of these systems for biomedical engineering. Microcapsules fabricated in dispersions cannot be easily transferred to supporting substrates in a controlled manner similarly to solid nano- and microparticles. Highly ordered arrays of microcontainers can aid in high-throughput analysis and fast optimization of sensing protocols and delivery conditions by providing a prospective platform for addressable microcapsulating arrays.[32,33]

The fabrication of 3D microcontainers and their arrays is typically achieved using complex, multistep, lithographic processes combined with multistep assembly, where the patterns are fabricated on planar surfaces and upon release are folded along pre-patterned hinges facilitated by specific stimuli, or by ink-jet printing.[34–37] Recently, LbL hollow microchambers have been fabricated utilizing a photolithographic template with imprinted microwells coated by LbL films.[38–40] The choice of strong polyelectrolytes available for stable sidewalls is a challenge of this approach.[41,42] Furthermore, the options for encapsulated contents are strongly restricted by the chemicals, solvents or temperatures used during fabrication and by the limited compatibility between the solvents used for loading and the wall assembly of the microcontainers. Firm sealing is a also critical problem for long-term protection of entrapped materials and release.[43]

Herein, potentially addressable arrays of self-formed "micro-bubble" constructs are successfully fabricated by confining frontal dissolution of a sacrificial material and encapsulating of the material in conformal silk fibroin microscopic sheets. The silk-coated "micro-bubble" constructs can encapsulate hydrophobic and hydrophilic materials as well as nanoparticles. These biocompatible and biodegradable micro-bubble constructs present a promising platform for spatial and controllable loading and locking material within large-scale arrays with addressable abilities. Silk fibroin materials with extraordinary mechanical

C. Ye, Prof. H. Dai
School of Light Industry Science and Engineering
Nanjing Forestry University
Nanjing, Jiangsu 210037, China
C. Ye, Dr. D. D. Kulkarni, Prof. V. V. Tsukruk
School of Materials Science and Engineering
Georgia Institute of Technology
Atlanta, GA 30332, USA
E-mail: Vladimir@mse.gatech.edu

DOI: 10.1002/adfm.201400254

properties are used in this study to ensure mechanical robustness of the conformal coatings. Silk fibroin is composed of natural amino acids [44,45] and is biocompatible, biodegradable, and mechanically stable.[46–49] The secondary structure of silk can be further stabilized by the formation of antiparallel β-sheet nanocrystals, which is utilized in this study to fabricate robust silk bilayers.[50,51]

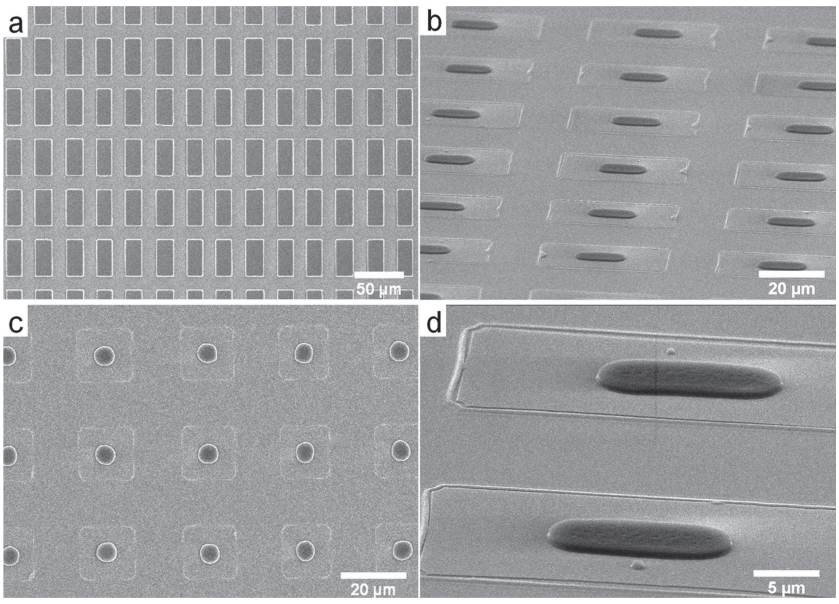

Figure 1. Morphology of silk micro-bubble constructs. a) SEM image of a large scale silk sheet array. b,c) Formation of micro-bubble array after acetone-induced PS layer dissolution under silk sheets with aspect ratio 2:1 (b) and 1:1 (c). d) High resolution SEM images of elongated micro-bubble constructs.

2. Results and Discussion

2.1. Silk-Coated Micro-Bubble Constructs

The SA-LbL silk β-sheet film exhibited an increment of 2.5 nm per layer. The methanol treatment of silk surfaces resulted in the transformation to the silk II secondary structure (β-sheets) that has been utilized in this study in order to stabilize the ultrathin silk films.[50,51] The resulting uniform silk films with thickness of tens to hundreds of nanometers were subjected to photolithography and dry etching to fabricate large-scale, highly ordered microscopic rectangular silk sheets with precisely designed dimensions (Figure 9). Furthermore, exposing patterned silk sheets to acetone resulted in the top photoresist layer and the underlying PS layer dissolving and the silk sheets collapsing but not lifting off. Surprisingly, we discovered that during this release process and dissolution of the polymer supporting layer, the silk sheets "grab and seal" the supporting polymer material in discrete regions, which are called "micro-bubble" constructs.

2.2. Morphology of the Silk Micro-Bubble Constructs

The SEM images of arrays of silk microscopic sheets with different aspect ratios reveal remarkably consistent ultrathin rectangular regions and corresponding arrays of micro-bubble constructs that replace the original pattern after solvent processing and dissolution of the supporting layer (**Figure 1**). Moreover, the shape of the micro-bubbles can be readily tuned by controlling the aspect ratio of the silk sheets. Specifically, the micro-bubbles change from a round to an ellipsoidal shape with a change in the aspect ratio of the initial silk sheets from 1:1 to 2:1 (Figure 1b,c). The micro-bubble constructs maintained their shape upon drying without noticeable wrinkling or collapse, suggesting a compact and mostly solidified physical state in the final array (Figure 1d).

AFM images of silk sheets with dimensions 50 μm × 100 μm and a thickness of 114 ± 3 nm clearly show the overall cylindrical shape of a micro-bubble with a diameter of 9.5 ± 0.85 μm and a height of 1.5 ± 0.1 μm (**Figure 2**a,b). It is worth noting that the edge of the silk sheet shrunk from the original dimensions by about 1.4 μm along the edge (Figure 2a, insert image). This uniform and small (<3%) shrinkage corresponds to a total area reduction of about 400 μm^2 per sheet. This reduction in area is close to the additional surface area build-up around the elevated micro-bubbles (about 300 μm^2) which indicates there is a "surface material conservation" and uniform pulling of silk sheets to the central regions to accommodate the change in morphology. It is also important to note that the volume of the micro-bubble calculated from these dimensions is close to the volume of the initial PS supporting layer under the silk sheet (difference less than 5%). Thus, this high yield, highly effective, loss-free encapsulation process allows silk sheets to "grabbing and sealing" the whole material beneath them.

To confirm the contents, Raman spectra of the silk-polymer constructs were collected (Figure 2c–f). The Raman mapping obtained by integrating the intensity of the spectra between 1575–1660 cm^{-1}, corresponding to the C = C vibration of the phenyl ring in PS layer,[58] clearly demonstrated the highly localized presence of the PS material within the micro-bubble construct but not the surrounding region (Figure 2c). The mapping suggests that PS is predominantly assembled at the center of the pattern, within the micro-bubble region. On the other hand, Raman mapping of the characteristic peaks from the amid ring vibration of silk II (1210–1260 cm^{-1}) suggested that the silk material dominates the surrounding region (Figure 2d). The absence of the strong amide signal in the central micro-bubble region can be attributed to the significantly higher volume of the PS-containing micro-bubble (≈1.5 μm) compared to the topmost silk layer (≈190 nm).

The Raman spectra obtained directly from the micro-bubble region showed a typical PS spectrum with characteristic peaks around 1630 cm^{-1} attributed to the vibration of a carbon double bond (C = C) in phenyl ring (Figure 2e).[59] Meanwhile, the Raman spectra collected from the silk sheets demonstrate an amide III bond (1209–1273 cm^{-1}) which correspondeds to the C-H bending[60] and amide III random coil.[48] The peaks 1566 cm^{-1}, 1621 cm^{-1}, and 1675 cm^{-1} were attributed

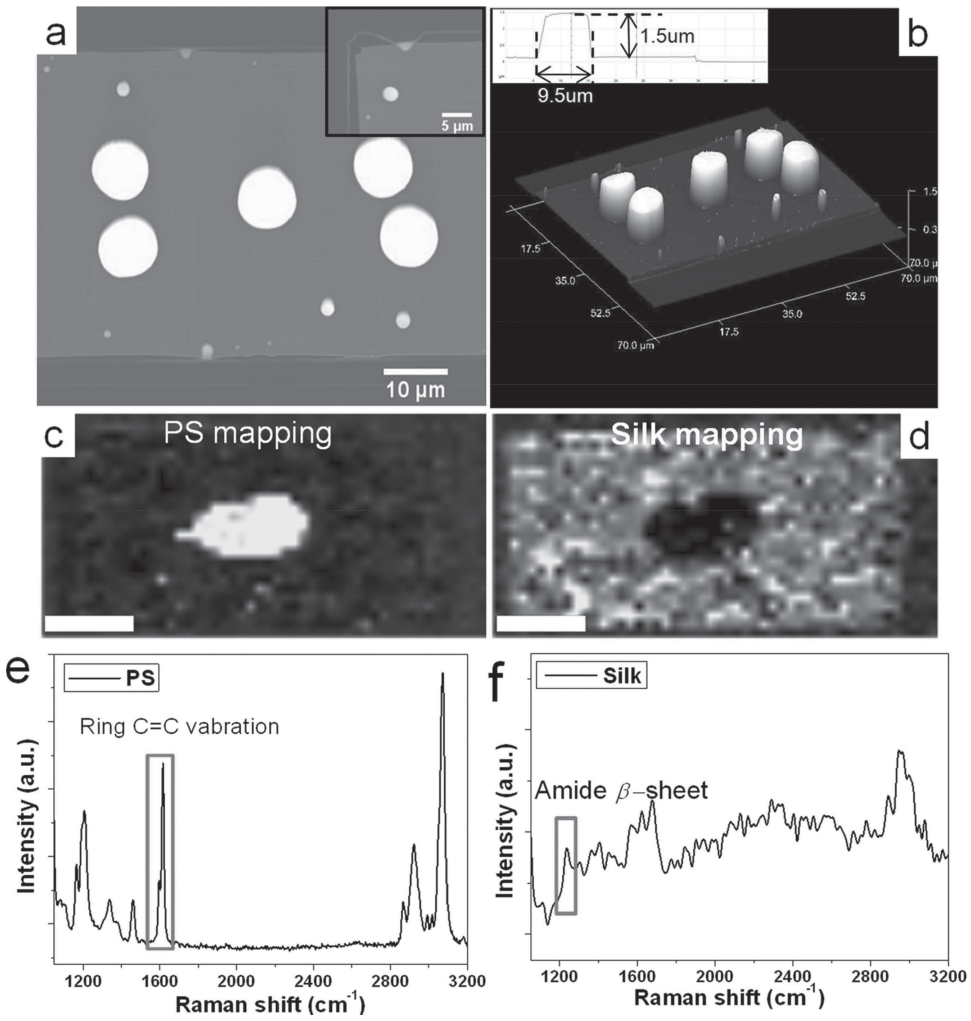

Figure 2. a,b) AFM topography images of silk-polymer micro-bubble constructs (*z*-scale: 2.5 μm). c) Raman map of the PS ring C = C vibration, scale bar: 20 μm. d) Raman map of the silk amide *β*-sheet vibration (1210–1260 cm^{-1}), scale bar: 20 μm. Raman scattering spectra collected from e) the micro-bubble region and f) surrounding areas.

to the (C–C) and (C = O) vibrations in amide I (Figure 2f).[60] The Raman spectra collected from the micro-bubble region and surrounding silk sheet area showed a peak around 2867–3075 cm^{-1} which corresponds to the symmetric and anti-symmetric (C–H) vibrations. Hence, Raman mapping clearly indicates that the PS material under the silk sheets is encapsulated within the central micro-bubble but is completely dissolved and removed in the surrounding regions.

2.3. Micro-Bubble Formation Process

In order to monitor the formation of micro-bubbles, we conducted direct observation of the processes after solvent addition with optical microscopy (**Figure 3**). These in-situ observations revealed that the exposure of PS-silk sheet arrays to acetone, a good solvent for PS, resulted in an immediate diffusion of the solution and dissolution of PS underneath the silk sheets through the periphery along the diagonals (Figure 3b). This selective penetration results in highly symmetric cross-shaped diffusion patterns under the silk sheets. At later stages, the PS and acetone mixture underneath the silk sheet gradually transformed into a central region with a spherical shape (Figure 3 c–i). We suggest that the capillary force originating from the gradual dissolution of the underlying PS layer facilitates the encapsulation process with the partially dissolved PS material displaced towards the central region and remaining entrapped underneath the collapsed silk sheets, as will be discussed below.

2.4. Control of the Micro-Bubble Pattern Formation

Next, we observed that the micro-bubble shape, number and position can be controlled by the silk sheet dimensions. First, the variation in the number of micro-bubbles that are formed beneath a single sheet was investigated within the patterned silk sheets with the same dimension (50 μm × 100 μm), but different sheet thicknesses (**Figure 4**).

Several smaller micro-bubbles were produced under ultrathin microscopic silk sheets (thickness of ≈8 nm) (Figure 4b).

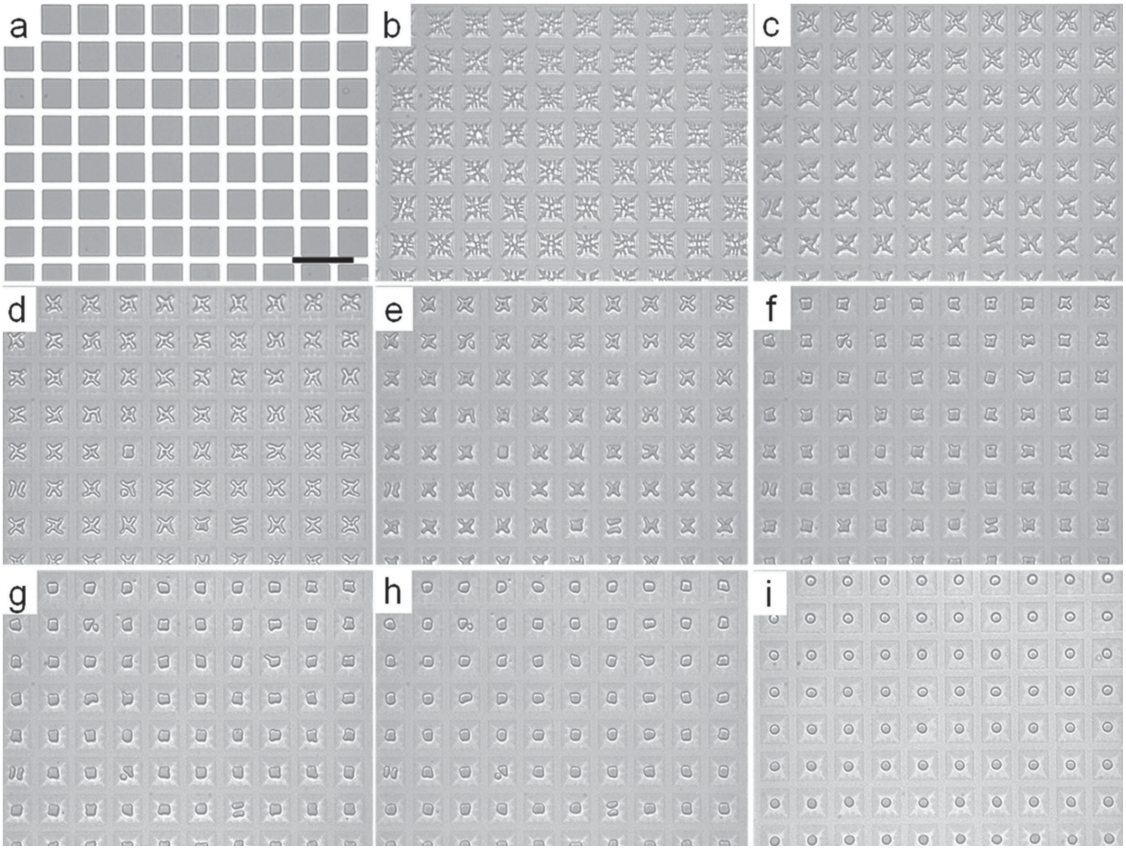

Figure 3. Optical microscopy images of the micro-bubble formation underneath the organized silk sheets during gradual dissolution of supporting PS layer and diffusion of solvent into the central region: a) initial silk sheet array at 0 s and after solvent addition: b) 33 s; c) 1 min 24 s; d) 2 min 11 s; e) 3 min 40 s; f) 5 min 30 s; g) 7 min 10 s; h) 10 min; i) 39 min; The scale bar is 100 μm for all panels.

Statistical analysis based-on more than 1000 silk sheets generated a distribution histogram of micro-bubble numbers, suggesting a peak value of 10 ± 2 micro-bubbles per sheet (Figure 4 b,c). Micrographs of silk sheets with increasing thicknesses clearly indicated a decrease in the number of micro-bubbles from 10 ± 2 to a single micro-bubble upon a thickness increase to 190 nm (Figure 4).

Second, the aspect ratio of silk sheets controls the number of micro-bubbles and their arrangement in the silk sheets as the aspect ratio varying from 1:1 to 1:8 (**Figure 5**). Single and round micro-bubbles are formed under silk sheets with a thickness of 85 ± 2 nm and an aspect ratio of 1:1 (Figure 5b). However, the increase of the aspect ratio of silk sheets resulted in the significant increase in the number of smaller micro-bubbles with a trend to the form chains at the highest aspect ratios (Figure 5). Overall, the number of micro-bubbles dramatically increased to 17 ± 3 for silk sheets with aspect ratio 1:8 (with dimension of 50 μm × 400 μm) (Figure 5h,i).

Furthermore, the shape and the number of micro-bubbles can also be controlled by the absolute lateral dimensions of the silk sheets (**Figure 6**). For instance, large and uniform single micro-bubbles with different shapes were observed for silk microscopic sheets with the width of 20 μm at various aspect ratios (Figure 6a–c). The shape of micro-bubble can be readily manipulated from round to ellipse by increasing the aspect ratio from 1:1 to 1:4 (Figure 6a–c).

However, the single large micro-bubble transformed into multiple and smaller micro-bubbles as the dimensions of the silk sheets increases, even if they hold the same aspect ratio (1: 2) and thickness (85 ± 3 nm) (Figure 6b,d).

2.5. Micro-Bubbles with Nanoparticles and Multicompartmental Morphology

Next, we tested the possibility of expanding the encapsulation capabilities of silk sheets to different supporting materials by employing fluorescence-labeled PS nano-beads (**Figure 7**a). Fluorescence microscopy confirmed that the targeted material (PS nano-beads) was primarily concentrated in these micro-bubble regions, while the bright field optical images revealed the same round micro-bubbles formed under silk sheets at these locations, thus confirming the encapsulation of PS nano-beads into these constructs.

Finally, we explored a "sandwiched" silk structure for the encapsulation of water-soluble FITC-Dextran (Figure 7b). Again, confocal fluorescent images clearly show the pre-programmed two-tiered micro-bubble morphology with two independently loaded compartments. The underlying PS polymer layer is encapsulated as a large single micro-bubble due to the thicker topmost coating. Furthermore, this large micro-bubble does not show fluorescence, ascribing to the lack of FITC-Dextran in the bottom layer independently encapsulated under first silk sheet (Figure 7b). In a strike contrast, the top labeled "sandwich" layer (FITC-Dextran and PS) formed several smaller micro-bubbles

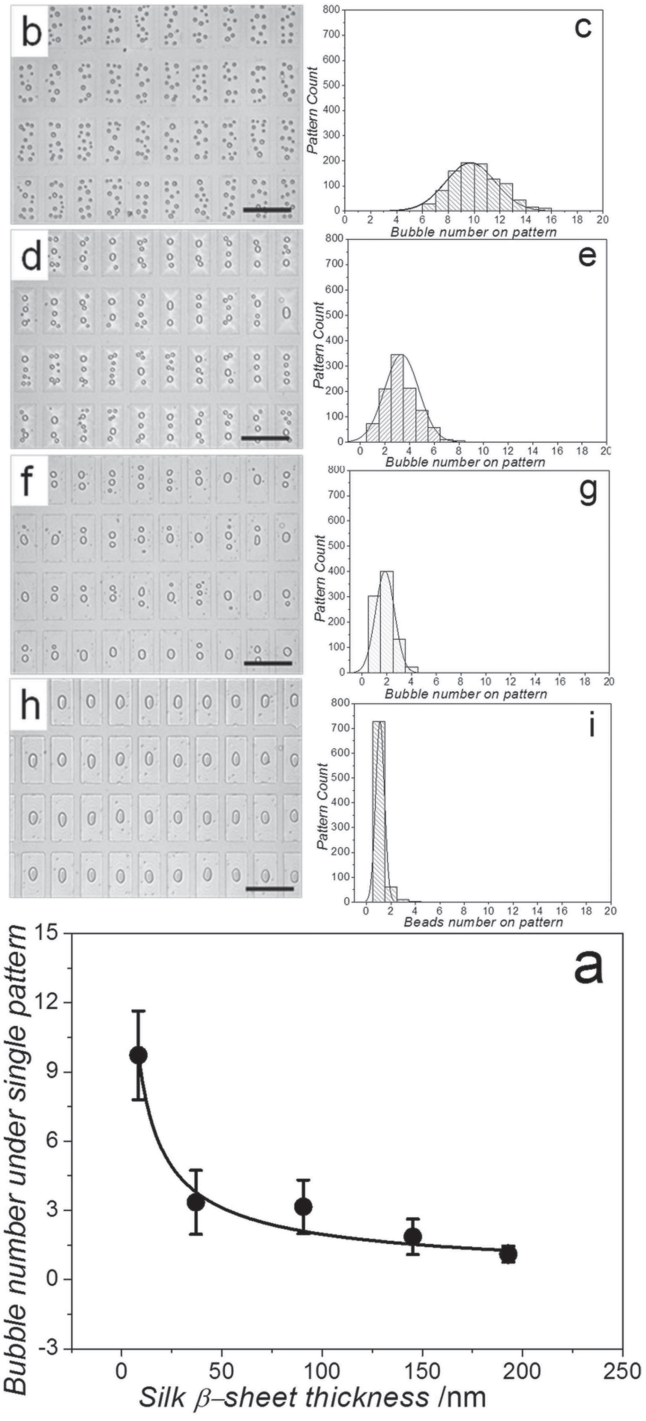

Figure 4. a) Variation of the number of micro-bubbles under a single silk sheet as a function of sheet thickness derived from optical images. Thickness: b) 8 nm, d) 37 nm, f) 145 nm, h) 190 nm. Scale bars: 100 µm. c,e,g,i) Statistical distribution of a number micro-bubbles within each silk sheet.

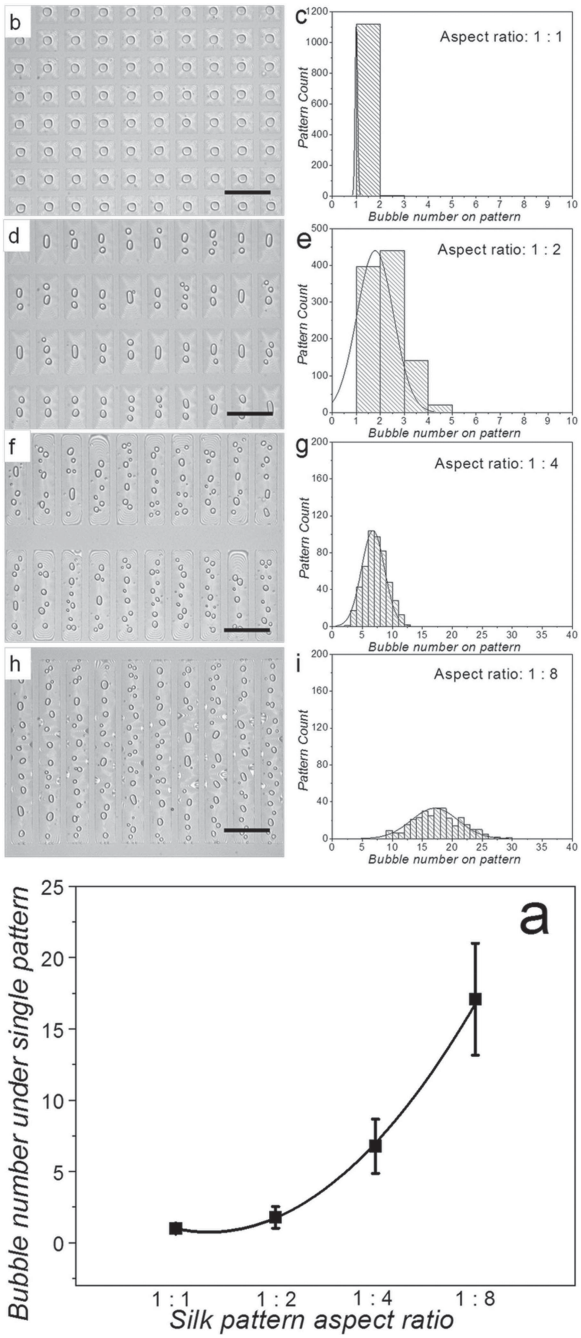

Figure 5. a) Variation of the number of micro-bubbles under silk sheets as a function of the aspect ratio (silk sheet width: 50 µm): at aspect ratios of b) 1:1; d) 1:2; f) 1:4; h) 1:8. Scale bars: 100 µm. And c,e,g,i) corresponding distributions.

with strong fluorescence across the entire sheet, suggesting that the labeled material from the second layer above the first silk sheet has been captured independently under the upper silk sheet. Overall, in this way a two-tiered or multicompartmental encapsulated structure with separately encapsulated non-labeled and labeled materials can be prepared.

2.6. The Mechanism of Encapsulation

The observations described above allow us to suggest the mechanism of the phenomenon revealed in this study and discuss the role of capillary forces, dissolution of the supporting layer, and diffusion of the solvent in the formation of the microbubbles under the silk sheets. By considering general trends in the diffusion/dissolution processes observed here, we suggest that when the patterns of silk sheets are exposed to acetone, the

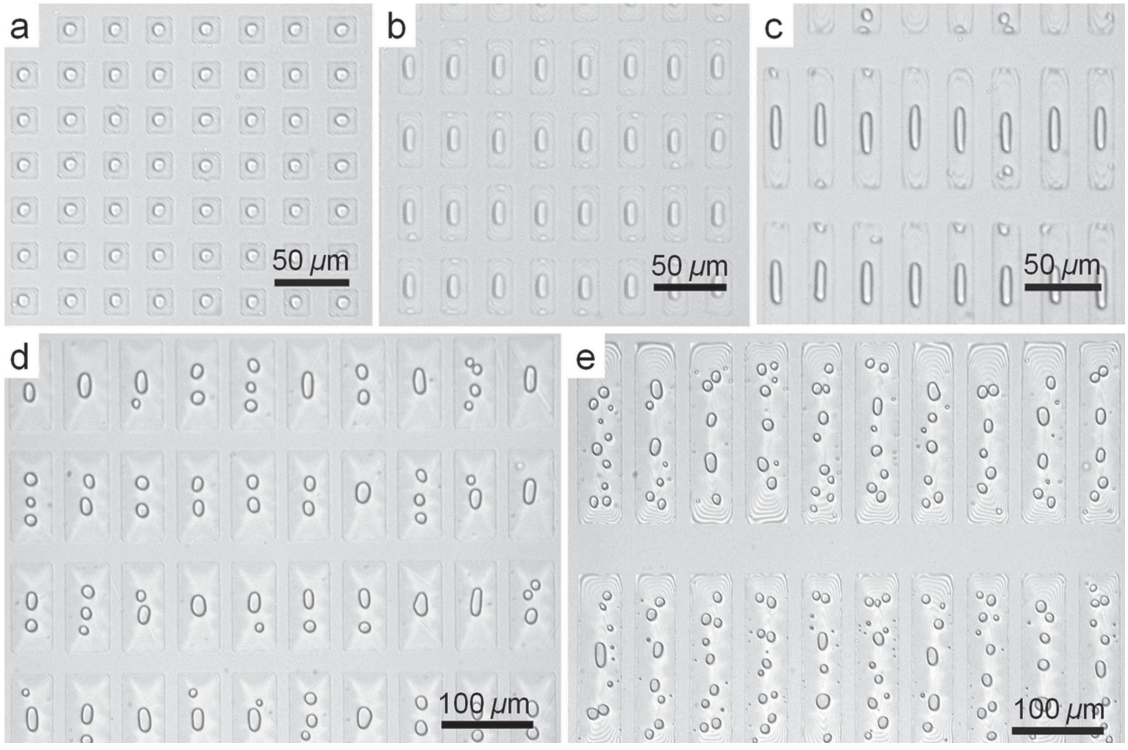

Figure 6. The shape of micro-bubbles as a function of silk sheet aspect ratio, a) 1:1, b) 1:2, c) 1:4 for silk sheet width of 20 μm. The variation of the number of micro-bubbles with the silk sheet lateral dimensions: b) 20 μm × 40 μm, d) 50 μm × 100 μm, e) 50 μm × 200 μm.

solvent diffuses underneath the silk sheets and starts swelling and dissolving the PS supporting layer starting at the edges of the microsheets (**Figure 8**a,b). As a result of the partial dissolution of the supporting PS layer, the topmost silk sheets, which preserve their integrity and flexibility in a poor solvent for silk, start losing support, collapse, and bend along the edges, following the solvent propagation front (Figure 8c). Silk sheets are forced to quickly bend by the capillary forces generated by the propagating meniscus until they meet the silicon oxide surface. Once the silk sheets reach the solid supporting surface,

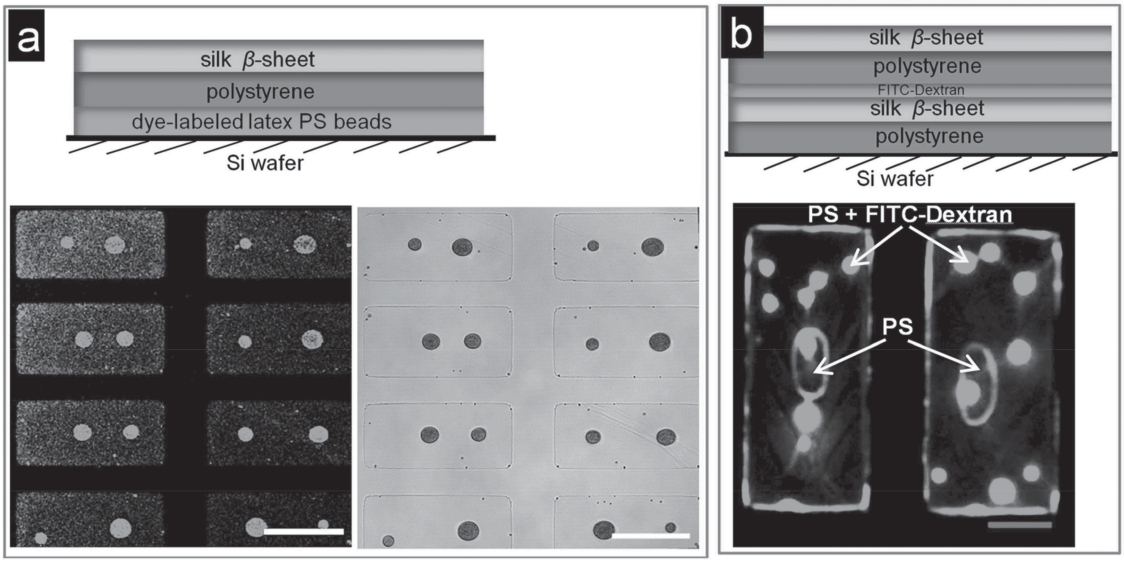

Figure 7. a) Layered silk micro-bubble construct for encapsulating dye-labeled latex beads, top image: schematic showing layered structure of the silk sheets, lower images: confocal images of encapsulated dye-labeled latex PS beads in micro-bubble, taken in fluorescence light (left) and transmission light (right) modes, scale bar: 50 μm. b) Encapsulation of FITC-Dextran with "sandwiched" micro-bubble structures (top schematics), lower image: confocal micrograph of the two-tiered micro-bubble structures, scale bar: 25 μm.

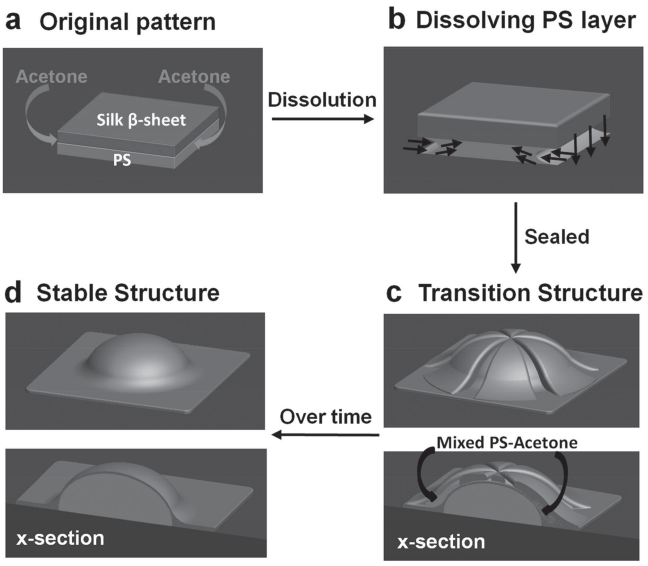

Figure 8. The evolution of micro-bubble construction as a result of the selective dissolution of the supporting layer, dissolution front propagation, bending of the silk coating, and sealing the gap behind the moving front.

the strong adherence between the silk sheets and the silica substrate effectively facilitates the firm sealing of PS-acetone mixture behind the propagating solvent front, cutting off further supply of solvent to the interior (Figure 8c).

The procedure includes two steps: first, capillary forces along the sheet edges causes the fast bending and collapsing of silk sheets, following by the formation of the strong adhesive sealing between the silk sheet edges and silicon oxide substrate along the sheet edges. Strong adhesion in the peripheral regions of the edges of the silk sheets on the substrate effectively seals the PS-acetone mixture in the central region underneath the silk sheets. These two steps are both critical for preserving the full dissolution of the PS supporting layer and resulting in the effective encapsulation of the forcefully migrated supporting material beneath the deformed silk coating (Figure 8d). Finally, when the silk sheets sealed the circumstance of the sheets completely, the entrapped PS-acetone mixture (highly swollen and partially dissolved PS material) reached an equilibrium state and adapted the lowest surface energy state, which is the simple dome-like shape of a central micro-bubble for the case of equidistant and symmetric diffusion paths (Figure 8d).

According to the principle of minimized surface energy, the preferred shape of micro-bubbles formed beneath the robust and deformable silk coating is spherical with a minimum specific surface area such as that observed in sheets of 1:1 aspect ratio. The low aspect ratio facilitates similar progression of the dissolution of the PS supporting layer to the central region from equidistantly distant edges. On the other hand, differences of the dissolution path along the long axes and short axes of sheets with high aspect ratios result in the formation of an ellipsoidal shape of the central micro-bubble. For high aspect ratios the central region further breaks into smaller round micro-bubbles for larger sheet dimensions.

To verify that the bending and collapse of the silk sheets can be facilitated by the phenomena suggested above, we consider the mechanical behavior of a supported silk sheet as a microscopic elastic plate undergoing external stress acting at the edges (Figure 8b). We ignore gravitational forces, which are insignificant for flat ultrathin microstructures.[61] We suggest that the capillary forces caused by the meniscus formed by the propagating fluidic front between the solid substrate and the sheet play the major role in the encapsulation process.[62] In order to evaluate the corresponding stress, P, we applied the Laplace equation for the slit-like flat gap:[63]

$$P = \frac{2\gamma}{x} \tag{1}$$

where γ is the surface tension of the acetone and x is the distance between two plates.

For the common separation between the silk sheet and the silicon substrate of 100 nm and the surface tension of acetone of 23.5 mN m^{-1},[64] the Laplace pressure is calculated to be 0.47 MPa. On the other hand, the theory of elastic stability of elastic plates under external stresses allows for the estimation of the limits of silk sheet stability under acting capillary forces. The sheets undergo fast bending (first order buckling phenomenon) only if the external load exceeds a critical stress, σ_{cr} which can be evaluated according to:[65]

$$\sigma_{cr} = \frac{\pi^2 E h^2}{12a^2\left(1-\upsilon^2\right)}\left(1+\frac{a^2}{b^2}\right) \tag{2}$$

where E is Young's modulus of silk, h is sheet thickness, a is the length and b is the width of the sheet, and υ is the Poisson's ratio.

As previously reported, the Young's modulus of silk β-sheet is around 6 GPa,[50] and the Poisson's ratio is 0.5 for an incompressible elastic material.[66] The calculated critical stress is in the range of 0.2 KPa to 0.24 MPa for the silk microscopic sheets with different thicknesses and lateral dimensions investigated in this work. Even the highest value of the critical stress required for thicker and smaller sheets is well below the applied Laplace pressure. Therefore, the Laplace capillary force at the edges of the silk sheets is strong enough to bend and collapse all silk structures fabricated in this study.

On the other hand, irreversible collapse with firm sealing occurs if the adhesive forces acting between the silk sheets and the silicon surface are larger than the critical stress for the sheet bending. This adhesion strength can be estimated through Dupré equation: [63]

$$W_{AB} = \gamma_A + \gamma_B - \gamma_{AB} \tag{3}$$

where W_{AB} represents the work necessary to separate a unit area of the interface AB into two interfaces (J), γ_A is the surface tension of silica-acetone interface, γ_B is the surface tension of silk-acetone interface, γ_{AB} is the surface tension of silica–silk interface. The work of adhesion can be further evaluated from the Girifalco-Good equation: [63]

$$W_{AB} = 2\sqrt{\gamma_A \gamma_B} \quad (4)$$

The work to separate a unit area of the silica–silk interface also can be considered as:

$$W_{AB} = Px \quad (5)$$

where P represents the adhesion between the silk sheet and silica, x is the separation between the silk sheet and Si. Inserting Equation (4) into (5), the adhesion strength can be calculated as:

$$P = \frac{2\sqrt{\gamma_A \gamma_B}}{x} \quad (6)$$

For simplification, the surface tension of silk–air interface and silica-air interface were used in Equation (6) instead of the surface tension of silk-acetone and silica-acetone interfaces.[67,68] Under these assumptions, the calculated adhesion strength is 3.3 MPa, which is much higher than the critical stress of silk sheet deformation, thus, confirming the irreversible adherence of the silk coating to the silica surface.

The lateral dimensions and the thickness of the silk sheets are important factors for determining the critical stress of the sheets according to Equation (2). One can predict that because the value of critical stress decreases with increasing sheet lateral dimensions, larger silk sheets are more prone to the collapse induced by the capillary forces. Hence, multiple micro-bubbles are formed for silk sheets with the same thickness but larger dimensions, as was indeed observed. Furthermore, the value of critical stress dramatically increased from 0.2 KPa to 120 KPa with an increase of the sheet thickness. Therefore, thicker silk sheets with smaller lateral dimensions are more stable, preventing the formation of multiple microbubbles during the dissolution process that was also observed in this study.

3. Conclusions

We have revealed a novel approach to fabricate ordered arrays of micro-bubble constructs from patterned silk microscopic sheets with self-encapsulation capabilities, which is facilitated by selective dissolution of the supporting layer. The dissolution front, which originates at the edges of the sheet, induces fast collapse of the sheet edges which, in turn, is followed by quick sealing of the interior material that prevents full dissolution of supporting materials. The number, dimensions, and shape of the micro-bubbles can be readily controlled by the geometry of the silk sheets, such as lateral dimensions, thickness and aspect ratio, which all affect the balance of dissolving and sealing processes. The highly ordered array of micro-bubbles and the "sandwich" constructions enable pre-programmed encapsulation and co-encapsulation of different materials in multicompartmental constructs, which presents a promising platform for the formation of ordered addressable arrays of robust microcontainers for spatial and timely encapsulation and release systems.

4. Experimental Section

Materials: Silk fibroin solution was prepared from *Bombyx mori* silkworm cocoons as reported in literature.[52] Briefly, cocoons were cleaned and split into small pieces and sericin was removed by boiling the cocoons for 1 h in 0.02 M Na_2CO_3 solution, and then rinsed thoroughly with Nanopure water. The extracted silk fibroin was dissolved in 9.3 M LiBr solution at 60 °C, yielding a 20% (w/v) solution. The solution was dialyzed in 10 000 MWCO Slide-A-Lyzer cassette against Nanopure water for 24 h. Finally, the silk fibroin aqueous solution was centrifuged three times at 9000 rpm, 5 °C for 20 min to remove impurities and aggregates that occurred during dialysis. The solution was diluted to 1 mg mL^{-1} and stored at 2 °C. Polystyrene (PS) with M_W = 250,000 was obtained from Polysciences. Carboxylate-modified polystyrene latex beads with yellow-green fluorescence with a diameter of 30 nm were received from Sigma as 2.5% (w/w) aqueous suspension. Fluorescent isothiocyanate-dextran (FITC-Dextran) was obtained from Sigma-Aldrich. The positive photoresist SC1813 and developer MF319 were supplied by Dow Chemical. Acetone, toluene and methanol were purchased from VWR international, LLC. All the water used in this study was Nanopure water with resistivity above 18.2 MΩ cm (Nanopure system, Barnstead). Single-side polished silicon wafers of the {100} orientation (University Wafer Co) were cut to a typical size of 10 mm × 20 mm and cleaned in a piranha solution as described elsewhere.[53]

Fabrication of Silk Fibroin Nano-Films: All the films were prepared by the spin-assisted layer-by-layer (SA-LbL) technique.[54,55] First, a PS layer was deposited on a silica wafer by spinning 2% solution in toluene at 3000 rpm for 30 s. Next, silk fibroin aqueous solution (1 mg mL^{-1}) was spun on the PS layer under the same conditions. After each silk layer, methanol was used to transfer the silk coil morphology to silk II structure with β-sheets, followed by a washing cycle with Nanopure water. This routine was repeated multiple times until the desired film thickness was reached. The thickness of a resulting silk film was measured using an M2000 ellipsometer (Woollam).

Preparation of Silk Micro-Bubble Constructs: Bilayer silk sheet micro-patterns were fabricated by employing a single exposure step photolithography process under cleanroom conditions (**Figure 9**). A

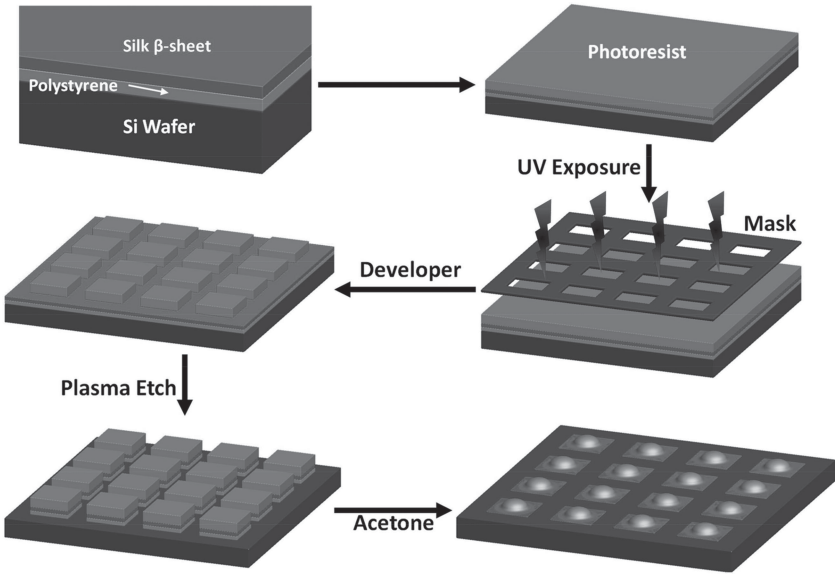

Figure 9. Fabrication procedure of micro-bubble construct arrays.

layer (thickness: 1.5 μm) of positive photoresist (SC1813) was spun onto the silk film. A photomask was used to facilitate selective exposure of the film to UV light. Following a further development procedure, the photoresist layer formed micro-patterns on the silk film, which protected the covered parts of silk as the film was subjected to plasma thermal reactive-ion etching (RIE) to remove the uncovered regions of the underlying silk film. Different photomasks were used to fabricate silk micro-sheets with different geometries and dimensions. Finally, the silk-polymer arrays were immersed in acetone solution to selective dissolution of supporting polymer layer and trigger the spontaneous formation of micro-bubble constructs (Figure 9).

Atomic Force Microscopy (AFM) and Scanning Electron Microscopy (SEM): The surface topography of the silk micro-bubble pattern was examined with AFM in the dry state.[56] The AFM images were collected from a Dimension-3000 AMF (Digital Instruments) in tapping mode using silicon V-shape cantilevers with a spring constant of 46 N m^{-1}. The vertical dimension of the micro-bubble was determined using the bearing analysis from the NanoScope software.[57] SEM was performed on a Hitachi S-3400-II scanning electron microscope at 10 KV. Before imaging, the samples were dried under vacuum and sputter-coated with a gold layer.

Optical Microscopy and Raman Scattering: The Raman spectra were obtained using a Witec (Alpha 300R) Confocal Raman Microscope equipped with a 514 nm Ar+ ion laser. The images were collected with a 50× objective (NA = 0.75), an integration time of 5 sec, and a spectral resolution of 4 cm^{-1}. The Raman spectra were obtained by averaging over 30 points over the selected region. Confocal images of the silk micro-bubble structures were obtained with a LSM 510 Vis confocal microscope equipped with 63× 1.4 oil immersion objective lens (Zeiss). The excitation/emission wavelengths were 488/515 nm. Optical images were collected during the dissolution of the supporting layer using a Leica DM4000 M optical microscope to record the formation of micro-bubbles. All the images were acquired using bright field mode at 10×, 20×, or 50× magnifications.

Acknowledgements

The authors appreciate the assistance and helpful discussions from Sidney T. Malak, Kesong Hu, Amir Dindar, Xing Liu, Dr. Mikkel A. Thomas and Dr. Ting Zhu. This work is supported by the Air Force Office for Scientific Research with FA9550–11–1–0233 and FA9550–09–1–0162 (BIONIC Center) Grants, China Scholarship Council grant 2010832447, and the priority academic program development of Jiangsu Higher education institutions, PAPD.

Received: January 23, 2014
Revised: February 24, 2014
Published online: April 9, 2014

[1] C. L. Randall, T. G. Leong, N. Bassik, D. H. Gracias, *Adv. Drug Delivery Rev.* **2007**, *59*, 547.
[2] T. G. Leong, A. M. Zarafshar, D. H. Gracias, *Small* **2010**, *6*, 792.
[3] M. A. Stuart, W. T. Huck, J. Genezer, M. Müller, C. Ober, M. Stamm, G. B. Sukhorukov, L. Szleifer, V. V. Tsukruk, M. Urban, F. Winnik, S. Zauscher, L. Luzinov, S. Minko, *Nat. Mater.* **2010**, *9*, 101.
[4] A. D. Dinsmore, M. F. Hsu, M. G. Nikolaides, M. Marques, A. R. Bausch, D. A. Weitz, *Science* **2002**, *298*, 1006.
[5] F. Caruso, R. A. Caruso, H. Möhwald, *Science* **1998**, *282*, 1111.
[6] G. B. Sukhorukov, H. Möhwald, *Trends Biotechnol.* **2007**, *25*, 93.
[7] J. T. Wilson, W. Cui, V. Kozlovskaya, E. Kharlampieva, D. Pan, Z. Qu, V. R. Krishnamurthy, J. Mets, V. Kumar, J. Wen, Y. Song, V. V. Tsukruk, E. L. Chaikof, *J. Am. Chem. Soc.* **2011**, *133*, 7054.
[8] V. Kozlovskaya, E. Kharlampieva, B. P. Khanal, P. Manna, E. R. Zubarev, V. V Tsukruk, *Chem. Mater.* **2008**, *20*, 7474.
[9] I. Drachuk, O. Shchepelina, M. O. Lisunova, S. Harbaugh, N. Kelley-Loughnane, M. Stone, V. V. Tsukruk, *ACS Nano* **2012**, *5*, 4266.
[10] I. Drachuk, M. K. Gupta, V. V. Tsukruk, *Adv. Funct. Mater.* **2013**, *36*, 4437.
[11] V. Kozlovskaya, E. Kharlampieva, S. Chang, R. Muhlbauer, V. V. Tsukruk, *Chem. Mater.* **2009**, *21*, 2158.
[12] E. Donath, G. B. Sukhorukov, F. Caruso, S. A. Davis, H. Möhwald, *Angew. Chem. Int. Ed.* **1998**, *37*, 2002.
[13] M. Delcea, H. Möhwald, A. Skirtach, *Adv. Drug Delivery Rev.* **2011**, *63*, 730.
[14] A. G. Skirtach, A. M. Yashchenok, H. Mohwald, *Chem. Commun.* **2011**, *47*, 12736
[15] C. Ye, O. Shchepelina, R. Calabrese, I. Drachuk, D. L. Kaplan, V. V. Tsukruk, *Biomacromolecules* **2011**, *12*, 4319.
[16] K. Köhler, H. Möhwald, G. B. Sukhorukov, *J. Phys. Chem. B* **2006**, *110*, 24002.
[17] A. S. Angelatos, B. Radt, F Caruso, *J. Phys. Chem. B* **2005**, *109*, 3071.
[18] N. Elsner, V. Kozlovskaya, S. A. Sukhishvili, A. Fery, *Soft Matter* **2006**, *2*, 966.
[19] Z. Zhu, S. A. Sukhishvili, *J. Mater. Chem.* **2012**, *22*, 7667.
[20] M. K. Park, K. Onishi, J. Locklin, F. Caruso, R. C. Advincula, *Langmuir* **2003**, *19*, 8550.
[21] V. Kozlovskaya, S. Ok, A. Sousa, M. Libera, S. A. Sukhishvili, *Macromolecules* **2003**, *36*, 8590.
[22] C. J. Ochs, G. K. Such, B. Städler, F. Caruso, *Biomacromolecules* **2008**, *9*, 3389.
[23] Z. P. Wang, Z. Q. Feng, C. Y. Gao, *Chem. Mater.* **2008**, *20*, 4194.
[24] M. Hamidi, A. Azadi, P. Rafiei, *Adv. Drug Delivery Rev.* **2008**, *60*, 1638.
[25] J. L. West, *Nat. Mater.* **2003**, *2*, 709.
[26] J. Feng, B. Wang, C. Gao, J. Shen, *Adv. Mater.* **2004**, *16*, 1940.
[27] B. Wang, Q. Zhao, F. Wang, C. Gao, *Angew. Chem. Int. ed.* **2006**, *45*, 1560.
[28] C. M. Andres, N. A. Kotov, *J. Am. Chem. Soc.* **2010**, *132*, 14496.
[29] J. Hiller, J. D. Mendelsohn, M. F. Rubner, *Nat. Mater.* **2002**, *1*, 59.
[30] R. Gunawidjaja, C. Jiang, H. Ko, V. V. Tsukruk, *Adv. Mater.* **2006**, *18*, 2895.
[31] H. Ko, C. Jiang, V. V. Tsukruk, *Chem. Mater.* **2005**, *17*, 5489.
[32] A. C. Grayson, R. S Shawgo, Y. Li, M. J. Cima, *Adv. Drug Delivery Rev.* **2004**, *56*, 173.
[33] J. T. Santini, M. J. Cima, R. A. Langer, *Nature* **1999**, *397*, 335.
[34] T. G. Leong, Z. Y. Gu, T. Koh, D. H. Gracias, *J. Am. Chem .Soc.* **2006**, *128*, 11336.
[35] G. Stoychev, S. Turcaud, J. W. C. Dunlpo, L. Ionov, *Adv. Funct. Mater.* **2013**, *23*, 2295.
[36] R. R. A. Syms, E. M. Yeatman, V. M. Bright, G. M. Whitesides, *J. Microelectromech. Syst.* **2003**, *12*, 287.
[37] R. Suntivich, O. Shchepelina, I. Choi, V. V. Tsukruk, *ACS Appl. Mater. Interfaces* **2012**, *6*, 3102.
[38] C. M. Andres, I. Larraza, T. Corrales, N. A. Kotov, *Adv. Mater.* **2012**, *24*, 4597.
[39] M. V. Kiryukhin, S. M. Man, A. Tonoyan, H. Y. Low, G. B. Sukhorukov, *Langmuir* **2012**, *28*, 5678.
[40] M. V. Kiryukhin, S. R. Gorelik, S. M. Man, G. S. Subramanian, M. N. Antipina, H. Y. Low, G. B. Sukhorukov, *Macromol. Rapid Commun.* **2013**, *34*, 87.
[41] M. V. Kiryukhin, S. M. Man, S. R. Gorelik, G. S. Subramanian, H. Y. Low, G. B. Suukhorukov, *Soft Matter* **2011**, *7*, 6550.
[42] J. S. Randhawa, T. G. Leong, N. Bassik, G. M. Stern, D. H. Gracias, *Proc. Natl. Acad. Sci. U.S.A.* **2009**, *106*, 703.
[43] K. C. Wood, N. S. Zacharia, D. J. Schmidt, S. N. Wrightman, B. J. Andaya, P. T. Hommond, *Proc. Natl. Acad. Sci. U.S.A.* **2008**, *105*, 2280.
[44] F. G. Omenetto, D. L. Kaplan, *Nat. Photonics* **2008**, *2*, 641.
[45] R. Lewis, *Chem. Rev.* **2006**, *106*, 3762.
[46] H. Shulha, C. W. Foo, D. L. Kaplan, V. V. Tsukruk, *Polymer* **2006**, *47*, 5821.
[47] H–L. Jin, D. L. Kaplan, *Nature* **2003**, *424*, 1057.

[48] E. Kharlampieva, V. Kozlovskaya, R. Gunawidjaja, V. V. Shevchenko, R. Vaia, R. R. Naik, D. L. Kaplan, V. V. Tsukruk, *Adv. Funct. Mater.* **2010**, *5*, 840.
[49] M. A. Serban, D. L. Kaplan, *Biomacromolecules* **2010**, *11*, 3406.
[50] C. Jiang, X. Wang, R. Gunawidjaja, Y. H. Lin, M. K. Gupta, D. L. Kaplan, R. R. Naik, V. V. Tsukruk, *Adv. Funct. Mater.* **2007**, *17*, 2229.
[51] O. Shchepelina, I. Drachuk, M. K. Gupta, J. Lin, V. V. Tsukruk, *Adv. Mater.* **2011**, *23*, 4655.
[52] S. Sofia, M. B. McCarthy, G. Gronowicz, D. L. Kaplan, *J. Biomed. Mater. Res.* **2001**, *1*, 139.
[53] V. Kozlovskaya, E. Kharlampieva, K. Jones, Z. Lin, V. V. Tsukruk, *Langmuir* **2010**, *26*, 7138.
[54] U.-J. Kim, J. Park, C. Li, H.-J. Jin, R. Valluzzi, D. L. Kaplan, *Biomacromelecules* **2004**, *5*, 786.
[55] K. Hu, M. K. Gupta, D. D. Kulkarni, V. V. Tsukruk, *Adv. Mater.* **2012**, *25*, 2301.
[56] M. E. McConney, S. Singamaneni, V. V. Tsukruk, *Polym. Rev.* **2010**, *50*, 235.
[57] N. Elsner, F. Dubreui, A. Fery, *Phys. Rev. E* **2004**, *69*, 031802/1.
[58] J. R. Anema, A. G. Brolo, A. Felten, C. Bittencourt, *J. Raman. Spectrosc.* **2010**, *41*, 745.
[59] A. Palm, *J. Phys. Chem.* **1951**, *55*, 1320.
[60] H. G. M. Edwarda, D. W. Fareweill, *J. Raman Spectrosc.* **1995**, *26*, 901.
[61] P. Roca-Cusachs, F. Rico, E. Martínez, J. Toset, R. Farré, D. Navajas, *Langmuir* **2005**, *21*, 5542.
[62] H. Namatsu, K. Kurihara, M. Nagase, K. Iwadate, K. Murase, *Appl. Phys. Lett.* **1995**, *66*, 2655.
[63] A. W. Adamson, A. P. Gast, *Physical chemistry of surfaces*, Wiley-VCH, New York, **1997**, pp 353–458.
[64] K. S. Howard, R. A. McAllister, *A.1.Ch.E. J.* **1957**, *3*, 325.
[65] S. P. Timoshenko, J. M. Gere, *Theory of elastic stability*, McGraw-Hill, Singapore, **1963**, pp 348–360.
[66] M. V. Kiryukhin, S. M. Man, A. V. Sadovoy, H. Y. Low, G. B. Sukhorukov, *Langmuir* **2011**, *27*, 8430.
[67] W. H. Park, W. S. Ha, H. Ito, T. Miyamoto, H. Inagaki, Y. Noishiki, *Fibers Polym.* **2001**, *2*, 58.
[68] B. J. Keene, *Surf. Interface Anal.* **1987**, *10*, 367.